JACS
JOURNAL OF THE AMERICAN CHEMICAL SOCIETY

Article

pubs.acs.org/JACS

PbI_2–HMPA Complex Pretreatment for Highly Reproducible and Efficient $CH_3NH_3PbI_3$ Perovskite Solar Cells

Yi Zhang,[†,‡,⊥] Peng Gao,[*,‡] Emad Oveisi,[§] Yonghui Lee,[‡] Quentin Jeangros,[∥] Giulia Grancini,[‡] Sanghyun Paek,[‡] Yaqing Feng,[*,†,⊥] and Mohammad Khaja Nazeeruddin[*,‡]

[†]School of Chemical Engineering and Technology, Tianjin University, Tianjin 300072, China
[‡]Group for Molecular Engineering of Functional Materials, EPFL Valais Wallis, CH-1951 Sion, Switzerland
[§]Interdisciplinary Centre for Electron Microscopy, EPFL, CH-1015 Lausanne, Switzerland
[∥]Photovoltaics and Thin Films Electronics Laboratory, EPFL Neuchâtel, CH-2002 Neuchâtel, Switzerland
[⊥]Collaborative Innovation Center of Chemical Science and Engineering, Tianjin 300072, China

Supporting Information

ABSTRACT: Interfacial engineering of the meso-TiO_2 surface through a modified sequential deposition procedure involving a novel PbI_2–HMPA complex pretreatment is conducted as a reproducible method for preparing $MAPbI_3$ based perovskite solar cells providing the highest efficiencies yet reported with the polymer HTM layer. Grazing-incidence X-ray diffraction depth profiling confirms the formation of a perovskite film with a PbI_2-rich region close to the electron transport layer (ETL) due to the strong interaction of HMPA with PbI_2, which successfully retarded the dissolution of the PbI_2 phase when depositing the perovskite layer on top. These results are further confirmed by energy-dispersive X-ray spectroscopy performed in a scanning transmission electron microscope, which reveals that the I/Pb ratio in samples treated with the complex is indeed reduced in the vicinity of the ETL contact when compared to samples without the treatment. The engineered interface leads to an average power conversion efficiency of 19.2% (reverse scan, standard deviation SD < 0.2) over 30 cells (best cell at 19.5% with high FF of 0.80).

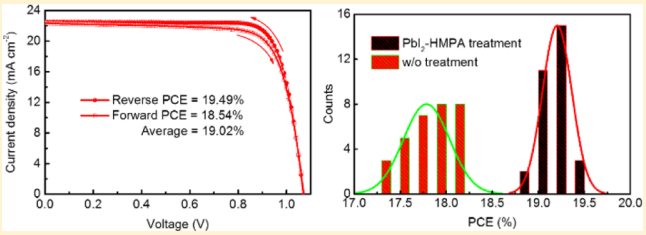

INTRODUCTION

Metal–organic halide perovskite solar cell (PSCs) have become the most important candidate for next generation thin film photovoltaics (PV) within an extremely short time scale.[1] Thanks to the sedulous efforts of device engineering (deposition protocol optimization, composition, solvent etc.),[2] the certificated photoconversion efficiency (PCE) has been ascending from 15%[3] to 22.1%[4] from 2013 to 2016. With all uniquely desirable features like high absorption coefficients, high charge carrier mobility, and diffusion lengths, as well as solution processability, etc., in one material, the hybrid halide perovskites have become the most promising all-round player for low cost optoelectronics.[5−9] Due to the "soft" nature of this hybrid halide perovskite material,[10] the photovoltaic properties of the corresponding PV devices are strongly dependent on the fabrication parameters,[11−13] deposition procedures,[14] hole/electron selective contact layers,[15] nanostructure of the scaffold layers,[16] interfacial microstructures,[17,18] as well as crystal lattice orientation of the perovskite compounds.[19] Among the successful device engineering methods, the use of non-stoichiometric precursor solution with excess PbI_2 has been proven to improve efficiency, and results have been reproduced by different laboratories to fabricate devices with efficiencies constantly higher than that of stoichiometric reference cells.[20−22] Despite controversy about the role and mechanism of excess PbI_2 behind the enhanced solar cell performance,[23] it is generally believed that it improves the crystallite growth of the capping layer, suppresses nonradiative recombination, and finally reduces hysteresis. Actually, long before the non-stoichiometric recipe was used, the benefits of excess PbI_2 have been found in either postannealed one-step deposited perovskite films[24−26] or from incomplete conversion in a two-step preparation.[18,27−30] Depending on the fabrication method, speculations about the way of existence of the PbI_2 phase inside a perovskite polycrystalline film have been made: PbI_2 is retained (i) at the interface between the metal oxide and perovskite phase;[25,31] and/or (ii) within the grain boundaries of perovskite crystallite.[21,24] Very recently, one combined experimental and computational study from our group concluded that with the nonstoichiometric recipe the excess PbI_2 may predominantly be located at the interface with TiO_2.[31]

Among the reported device engineering protocols, there is no controllable method to intentionally introduce PbI_2 only between the perovskite and electron transporting layers. It is known that the main group compound PbI_2 behaves like a Lewis acid and tends to form adducts by reacting with the

Received: August 12, 2016
Published: October 10, 2016

DOI: 10.1021/jacs.6b08347
J. Am. Chem. Soc. 2016, 138, 14380−14387

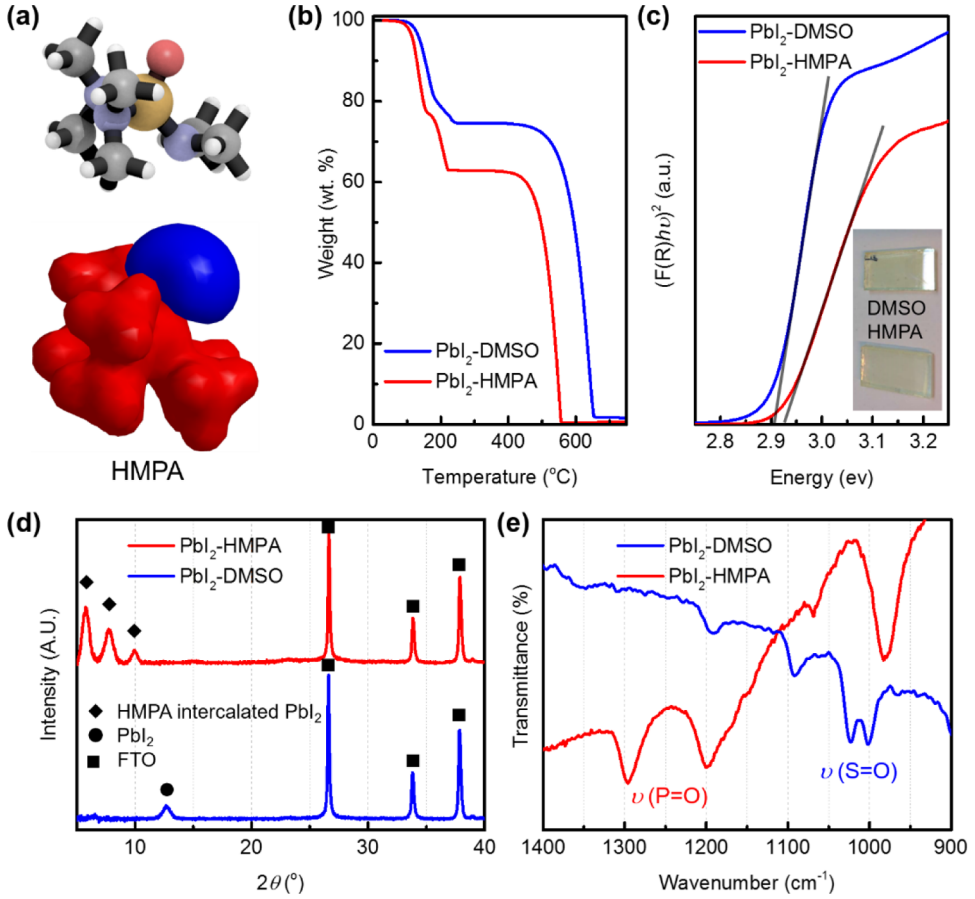

Figure 1. (a) Molecular model of HMPA and its molecular electrostatic potential calculated on the B3LYP 6-311(g, d) level; (b) thermogravimetric (TGA) analysis of different PbI_2−solvent complexes. (c) Diffuse reflectance transformed Kubelka−Munk spectra, (d) XRD patterns, and (e) Fourier transform infrared spectrometer (FTIR) of DMSO and HMPA based PbI_2 films.

Lewis base like oxygen, sulfur, or nitrogen containing polar aprotic solvents.[32] So far, Lewis base solvents like dimethylformamide (DMF),[33] dimethyl sulfoxide (DMSO),[34−37] and *N*-methyl-pyrrolidone (NMP)[38] have been successfully used to deposit PbI_2 or perovskite in the process of PSCs. On the other hand, anatase TiO_2 has Lewis-acid sites on the surface which is also ready to interact with an electron-pair donating Lewis base with oxygen, sulfur, and nitrogen donors.[39] Therefore, an ideal Lewis base would induce a stronger interfacial coupling at the interface of TiO_2 and PbI_2 and immobilize the PbI_2 phase on the surface for enhanced device performance.

EXPERIMENTAL SECTION

Device Fabrication. Chemically etched FTO glass (Nippon Sheet Glass) was cleaned with detergent solution, acetone, and isopropanol. To form a 20−25 nm thick TiO_2 blocking layer, diluted titanium diisopropoxide bis(acetylacetonate) (TAA) solution (Sigma-Aldrich) in ethanol (0.2 mL of TAA in 6 mL of anhydrous ethanol) was sprayed at 450 °C. A 200 nm mesoporous TiO_2 was coated on the substrate by spin-coating at a speed of 2000 rpm for 10 s with a ramp-up of 1000 rpm s^{-1} from a commercially available TiO_2 paste (Dyesol-30NRD) in ethanol. The weight ratio of TiO_2 paste to ethanol is 7:1. After spin-coating, the substrate was immediately dried on a hot plate at 80 °C, and the substrates were then sintered at 500 °C for 20 min before the deposition of the active layer. The PbI_2 precursor solution was prepared by spin-coating 0.1 M of PbI_2 in hexamethylphosphoramide (HMPA) on the ETL substrates at 3000 rpm for 15 s and annealed at 100 °C for 5 min. The $MAPbI_3$ precursor solution was prepared by mixing 1.2 M of PbI_2 and methylammonium iodide (MAI) in DMSO, which was then successively spin-coated on the substrates at 1000 rpm for 10 s and 5000 rpm for 30 s, respectively. A 100 μL portion of chlorobenzene was dropped over 10 s at 5000 rpm. $MAPbI_3$ films were annealed at 100 °C for 20 min. The HTM solution was prepared by dissolving 10 mg of poly(triarylamine) (PTAA) (Emindex) with additives in 1 mL of toluene. As additives, 7.5 μL of Li-bis(trifluoromethanesulfonyl) imide from the stock solution (170 mg in 1 mL of acetonitrile) and 4 μL of 4-tertbutylpyridine were added. The hole transporting material (HTM) layer was formed by spin-coating the solution at 3000 rpm for 15 s, and followed by the deposition of the 80 nm thick Au electrode by a thermal evaporation. All of the preparative work to deposit perovskite and PTAA was done inside a glovebox filled with nitrogen to minimize the influence of moisture.

XRD and Grazing-Incidence X-ray Diffraction (GI-XRD). XRD was performed using a D8 Advance diffractometer (Bruker AXS) model in an angle range of 2θ = 5−40° or 10−30° (Bruker Corporation, Billerica, MA).

Grazing-Incidence X-ray Diffraction (GI-XRD) Depth Profiling Analysis. The geometry is referred to as asymmetric Bragg geometry. In this work, a Göbel mirror was used for the incident beam, and thus, only the diffracted beam is collimated by a Soller-slit assembly. In a comparison with a focusing Bragg−Brentano geometry, the spectral resolution is usually reduced in this mode. A higher resolution is difficult to achieve with a laboratory setup, at least not within a reasonable time frame for the spectral acquisition process. The XRD measurements reported here were carried out on a D8 Advance diffractometer (Bruker AXS) equipped with parallel-beam optics on the primary side, Soller slits in front of the detector, and an Eularian cradle. Incident angles (ω) are in the range from 1° to 3°. Due to the limitation of instrument accuracy, it is hard to obtain the

DOI: 10.1021/jacs.6b08347
J. Am. Chem. Soc. 2016, 138, 14380−14387

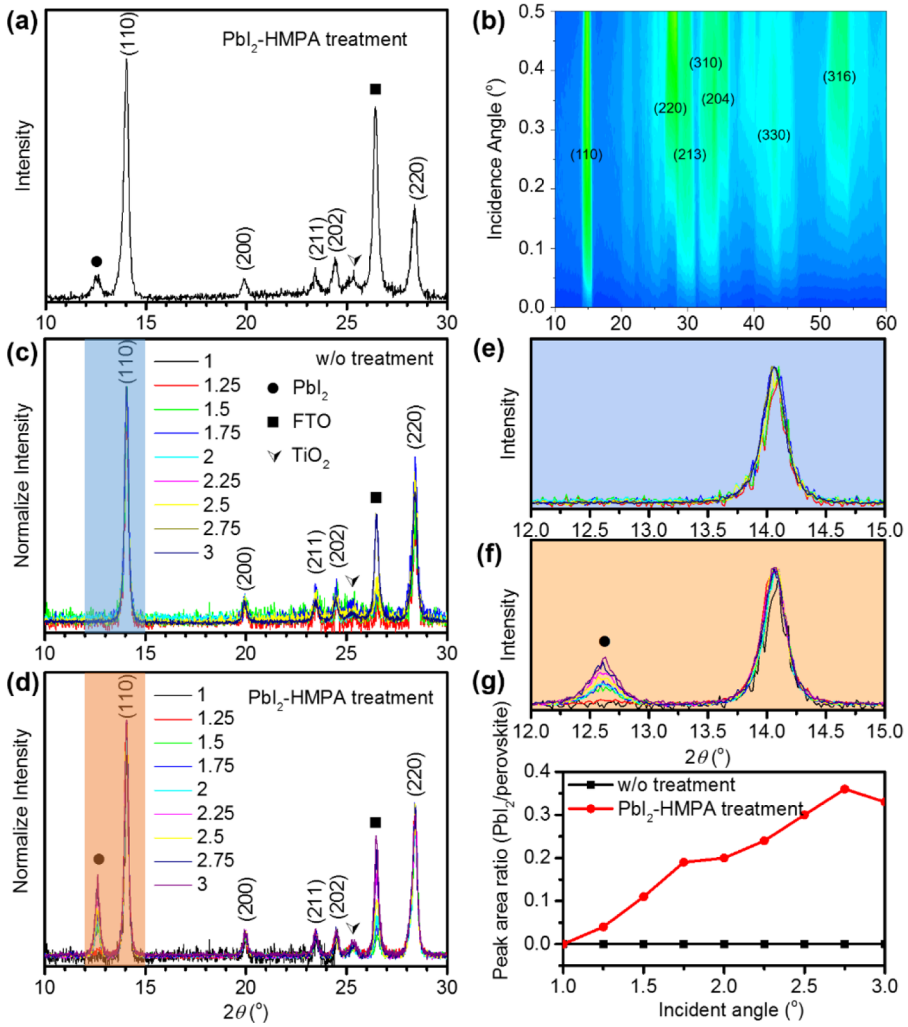

Figure 2. (a) Coupled 2θ XRD pattern of the perovskite films formed on a PbI_2–HMPA treated mesoporous TiO_2. (b) 2D GI-XRD intensity contour plots of the perovskite film with PbI_2–HMPA treatment (incidence angle from 0.02 to 0.5°). (c, d) 1D GI-XRD pattern obtained with incident angles in the range from 1° to 3° on film (c) without treatment and (d) with the PbI_2–HMPA treatment. (e, f) Highlighted diffraction profiles of the PbI_2 (001) and $MAPbI_3$ (110) reflections in the 2θ range from 12° to 15° for c and d, respectively. (g) The peak area ratio curves of the (001) reflection of PbI_2 and the (110) reflection $MAPbI_3$ of perovskite with different films with different incidence angles. All of the films have a structure of perovskite/TiO_2/FTO with depth gradient, and the incidence angle was varied from 0.02° to 0.5° or 1° to 3°, while all other parameters were held constant.

XRD curves in which the incidence angle is less than 1°. To understand the film surface information, synchrotron radiation is applied to these samples.

Low angle grazing-incidence X-ray diffraction (GI-XRD) analysis with incident angles in the range from 0.02° to 0.5° was performed at beamline BM01A (The Swiss-Norwegian Beamlines) of the European Synchrotron Radiation Facility. Incidence angles (ω) of 0.02–0.5° are selected to be below the critical angle of total external reflection of FTO but above that of perovskite.

RESULTS AND DISCUSSION

In this work, we demonstrate a modified sequential deposition method that involves the pretreatment of the mesoporous TiO_2 with PbI_2 solution in hexamethylphosphoramide (HMPA) and final deposition of methylammonium lead iodide ($MAPbI_3$) solution in DMSO. HMPA is a strong Lewis basic donor-solvent with a much higher electron-pair donating ability (e.g., the Gutmann's donor number DN = 38.8) than that of DMSO (DN = 29.8) and of DMF (DN = 26.6).[40,41] Therefore, the metal complexation is enhanced in HMPA over DMF and DMSO.[42] By using such strong Lewis basic donor-solvent, we expect an enhanced interaction of the solvent molecules with both PbI_2 and TiO_2, which will be beneficial to the final performance of the devices. With a combination of grazing-incidence X-ray diffraction (GI-XRD) depth profile, time-resolved photoluminescence (TR-PL), and energy-dispersive X-ray analysis in scanning transmission electron microscope (EDX-STEM), we find that the new Lewis basic donor-solvent can effectively retard the redissolution of predeposited PbI_2 and form an enriched PbI_2 region within the mesoporous TiO_2. Quantitative EDX elemental mapping performed on the cross sections of two PSCs after PV measurement under bias revealed a balanced atomic composition throughout the depth of the PSC layer compared to the reference film, which has a $MAPbI_3$-rich composition close to the TiO_2. Thus, we believe that the use of PbI_2–HMPA pretreatment on TiO_2 anode represents a simple and effective strategy for enhancing the interaction between TiO_2 and perovskite and subsequently device performance for PSC development. In the presence of the PbI_2–HMPA pretreatment, we realized a record high average

DOI: 10.1021/jacs.6b08347
J. Am. Chem. Soc. 2016, 138, 14380–14387

efficiency of 19.2% and best efficiency of 19.5% using poly(triarylamine) (PTAA) as hole transporting material.

The HMPA molecule has a pyramidal structure, the P═O bond of which is polar with an ionic character of approximately 50% (Figure 1a). The high electron density on the oxygen site gives rise to a large dipole moment and an unusually high basicity (Figure 1a).[43] PbI_2−HMPA as an off white solid forms when cooling down a saturated solution of PbI_2 in HMPA. A thermogravimetric analysis (TGA) of this solid is shown in Figure 1b along with that of a PbI_2−DMSO complex to estimate the content of solvent molecules. Both complexes exhibit a two-step decomposition process. The weight-loss behavior of the PbI_2−DMSO complex (26% at 240 °C) is in agreement with previous studies indicating a composition of $PbI_2(DMSO)_2$.[35] The first decomposition stage of the PbI_2−HMPA complex finished at 158 °C with a weight loss of 23%, while the second step finishes at 225 °C with another loss of 14%. Composition of this new complex is calculated to be $PbI_2(HMPA)_{1.5}$. The slight decrease in decomposition temperature is possibly due to the smaller crystal size of the PbI_2−HMPA complex. Elemental analysis of the complex crystal yielded the following percentages by weight: H = 3.9%, C = 15.1%, and N = 8.5%, with a remainder of 72.5%, which are roughly in agreement with the calculated results for the corresponding element in the formula of $(C_6H_{18}N_3OP)_{1.5}PbI_2$ requiring H = 3.7%, C = 14.8%, N = 8.6%, and remainder of 72.9%.

Figure 1c shows the PbI_2−DMSO and PbI_2−HMPA covered TiO_2 films and their transformed Kubelka−Munk spectra.[44] The color of the two films is typical of Lewis base intercalated PbI_2. From the extrapolation of the linear part of the $[F(R)h\upsilon]^2$ plot, their bandgaps (E_g's) are determined to be 2.91 and 2.93 eV for PbI_2−DMSO and PbI_2−HMPA, respectively. Compared with that of pure PbI_2 (E_g = 2.35 eV),[18] their E_g's are much enlarged, within which the E_g of PbI_2−HMPA is slightly larger than that of PbI_2−DMSO.

The most striking difference between the two complexes can be seen in the XRD patterns (Figure 1d). As already reported, the PbI_2−DMSO film shows only a dramatically weakened peak at 12.7°.[34] However, PbI_2−HMPA shows three strong diffraction peaks at 5.7°, 7.7°, and 9.9°, which correspond to lattice spacings of 1.53, 1.14, and 0.89 nm, respectively. This indicates that the HMPA molecules were intercalated in the PbI_2 structure forming at least three types of crystal unit cells. Attempts to grow a single crystal based on PbI_2−HMPA did not find success so far. The scanning electron microscopy (SEM) images of the two films showed different crystallization behaviors (Figure S3). The PbI_2−HMPA complex form aggregated tiny needle type crystals on the surface. They cover the surface of TiO_2 as a noncontinuous film with many pinholes inside. FTIR spectroscopy is conducted to provide collateral evidence of complex formation. The υ(S═O) at 1023 cm^{-1} in Figure 1e is consistent with previous reports about the PbI_2−DMSO complex.[32] In the case of PbI_2−HMPA, the stretching vibration of P═O in phosphoramide (υ(P═O)) appears at 1200 and 1296 cm^{-1}. ^{31}P NMR of the complex is given in Figure S1.

As mentioned earlier, after the deposition of PbI_2−Lewis base complex, the stoichiometric perovskite precursor solution in DMSO was spin-coated on top. The PbI_2−DMSO complex is readily dissolved when the perovskite layer is deposited, so in this study we concentrated on the PbI_2−HMPA treated film and compared it to the nontreated reference film. As evidenced from the coupled 2θ XRD pattern shown in Figure 2a, the small diffraction peak at 12.7° indicates the existence of the PbI_2 phase inside the film. This is similar to the case where a nonstoichiometric perovskite solution was used.[22] In order to confirm the unique effect of the PbI_2−HMPA treatment on the perovskite layer, synchrotron based grazing-incidence X-ray diffraction (GI-XRD) was used to provide sufficient scattering signal under extremely low incidence angle. GI-XRD measurements were performed at the Swiss-Norwegian Beamlines BM01A beamline at the European Synchrotron Radiation Facility. Diffraction information was collected from the incidence angles (ω's) of 0.02−0.5°, which are below the critical angle of total external reflection for FTO but above that of the perovskite (Figure 2b). At these incidence angles, the evanescent wave penetrating depth of X-rays is limited, so most of the scattering signal comes from the top layers. It is worth noting that, after indexing the scattering pattern, unexpectedly, no PbI_2 diffraction was detected. This is significantly different from the coupled 2θ XRD pattern indicating that the redissolution of PbI_2−HMPA phase is limited.

Given the limitation of the XRD equipment in our lab, the film composition profiles were acquired under incidence angles (ω) from 1° up to 3° as shown in Figure 2c,d, which shows a series of GI-XRD measurements taken from the perovskite films with and without the PbI_2−HMPA treatment. For comparison, the intensities of all of the diffraction peaks were normalized to the intensity of the (110) perovskite reflection. Compared to the coupled 2θ XRD pattern, the diffraction of FTO at 26.4° becomes much less significant when the angle of incidence is below 2.5°. The enlarged diffraction peaks of the (001) PbI_2 and (110) perovskite reflections of both films are highlighted in Figure 2e,f. Since the PbI_2−HMPA complex was deposited before spin-coating of the perovskite solution, a depth-dependent variation of the peak area ratios (PbI_2/perovskite) in the film is anticipated. For the film without PbI_2−HMPA treatment, PbI_2 does not appear under any incidence angle, and the PbI_2/perovskite peak area ratio curve equals 0 (Figure 2g), indicating that there is no breakdown phenomenon for the whole depth range of pure perovskite film. Meanwhile, for the perovskite film with the PbI_2−HMPA treatment, the intensity of the (001) PbI_2 peak varies and increases with the increasing incidence angle until 2.75°. This indicates that the PbI_2 phase mainly exists close to the FTO glass side and was not fully dissolved when spin-coating the DMSO solution of the perovskite precursor (Figure 2g). Overall, these results suggest the retarded dissolution process of the PbI_2−HMPA complex in DMSO.

The carrier lifetimes of the two kinds of films were investigated by a time-correlated single photon counting (TCSPC) technique as shown in Figure S2. The time-resolved PL lifetime was determined by measuring the PL decay at the peak emission of 770 nm with an excitation at 460 nm, and the perovskite PL dynamics was compared with and without the HMPA treatment. Note that we intentionally chose to use the SiO_2 as an insulating mesoporous substrate to get rid of any injection process. In a comparison with the reference film, we observed that the PL lifetime is shortened with the PbI_2−HMPA treated film. In agreement with previous work,[21] this might indicate the presence of a PbI_2-rich phase, which can induce quenching in the recombination dynamics.

PTAA as the most popular polymer hole transporting material was spin coated from its solution in toluene on to the perovskite layer, and a gold electrode was evaporated to form

DOI: 10.1021/jacs.6b08347
J. Am. Chem. Soc. 2016, 138, 14380−14387

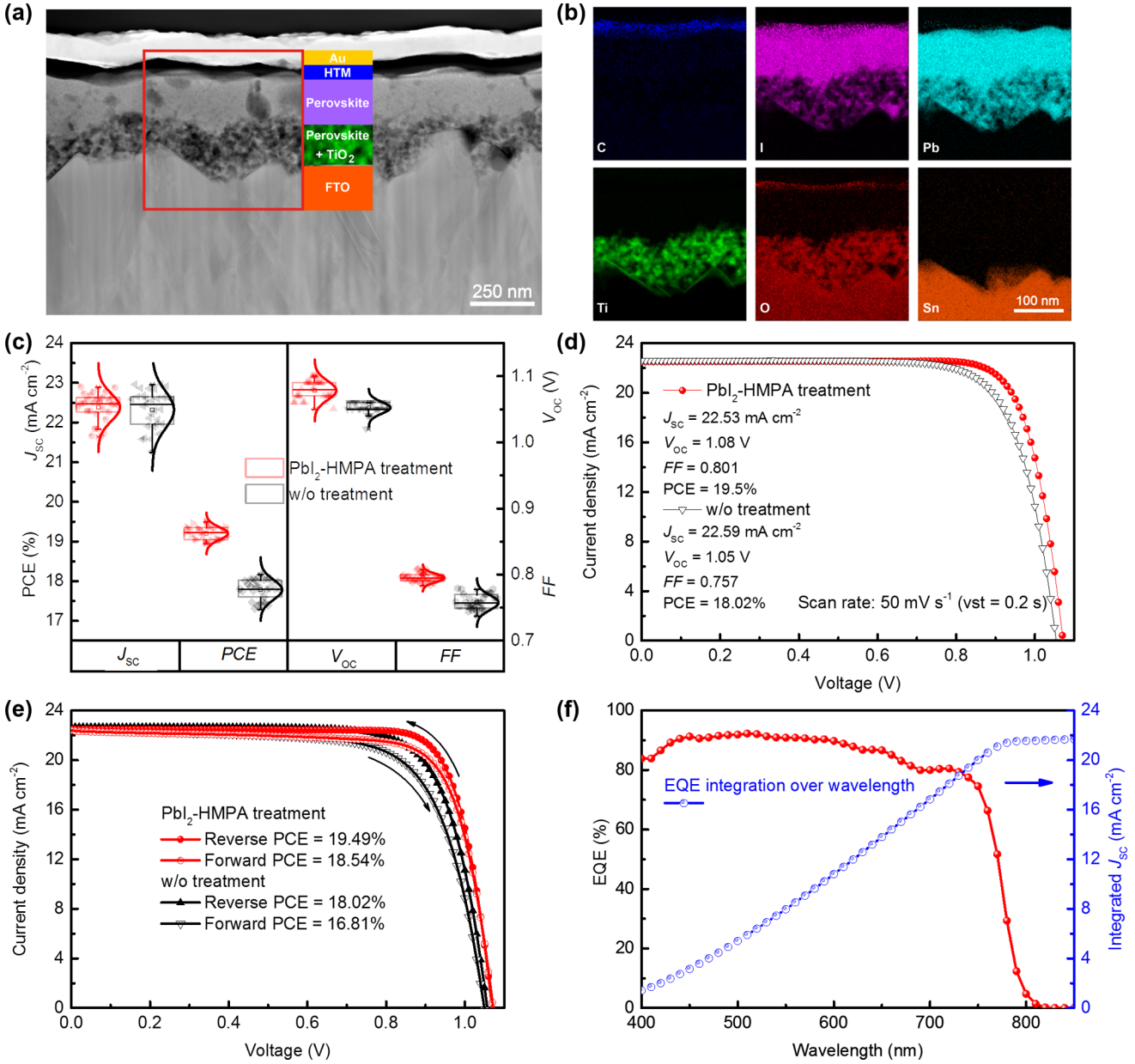

Figure 3. (a) Cross-sectional STEM-HAADF image of the sample comprising the following layers: FTO/c-TiO_2/mp-TiO_2/perovskite/PTAA/Au. (b) EDX map showing the elemental (C, I, Pb, Ti, O, Sn) distribution in the area shown by a red rectangle in part a. (c) Statistical deviation of the photovoltaic parameters for solar cells with and without the PbI_2–HMPA treatment, respectively (30 different solar cells each). (d) *J*–*V* curves and (e) reverse and forward scanned *J*–*V* curves obtained from the best solar cells with and without PbI_2–HMPA treatment, respectively. (f) EQE spectra with the integrated J_{SC} based on the EQE data of the champion device.

the complete solar cell. The advantage of using PTAA over Spiro-OMeTAD is the fact the material cost can be reduced by 86% as the concentration is only 1/7 that of Spiro-OMeTAD.[22] The spatial distribution of elements in complete cells with and without the HMPA treatment was investigated by EDX-STEM. For that purpose, cross-sectional specimens that were extracted from the devices after they had been electrically characterized using the conventional focused ion beam (FIB) lift-out method. The final Ga thinning parameters were 5 kV and 80 pA.[45] To minimize exposure of the lamellae to air, the EDX-STEM analyses were performed just after the FIB preparation, and the exposure to air exposure was kept below 3 min.

Figure 3a,b represents the STEM-HAADF (high angle annular dark field) micrographs and associated EDX elemental maps (C, I, Pb, Ti, O, Sn) of a cross-sectional views of the device (see Supporting Information (SI) for all experimental details). The total thickness of the capping layer and mesoporous layer is about 480 nm, while the PTAA based HTM has a thickness of 50 nm, which is much smaller than usual Spiro-OMeTAD thickness (normally 80 nm). The homogeneous distribution of I and Pb indicates a good infiltration of the two elements inside the mesoporous TiO_2.

A total of 60 solar cells in two groups were fabricated under the same conditions: one group was prepared with the PbI_2–HMPA treatment and the other without. Figure 3c demonstrates the statistical distribution of all four photovoltaic parameters of the two groups of solar cells showing the reproducibility of each condition. In the case of the PbI_2–

DOI: 10.1021/jacs.6b08347
J. Am. Chem. Soc. 2016, 138, 14380–14387

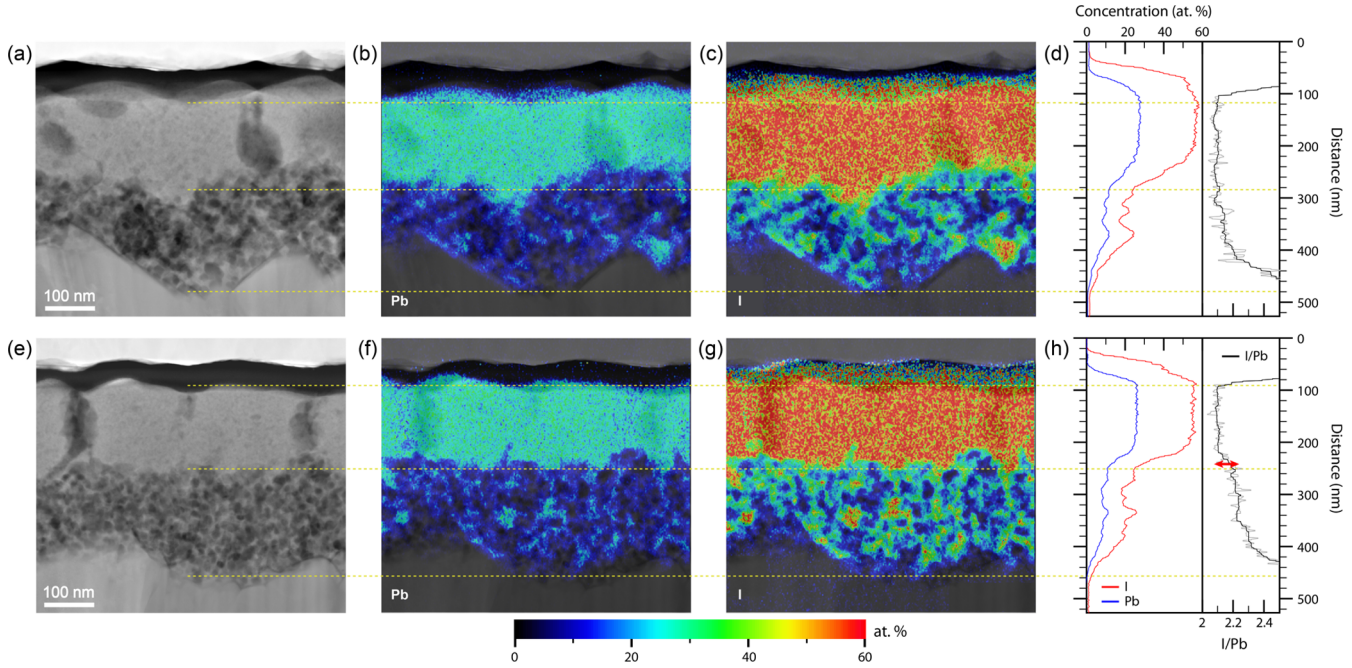

Figure 4. STEM-HAADF images (a, e) and associated quantitative EDX elemental maps (b, c, f, g) and line scans (at. %) for lead and iodine (d, h). The variation of the iodine to lead ratio over the mesoporous and perovskite layers is shown in part d for a cell with the PbI_2–HMPA treatment and in part h for a cell without the treatment.

HMPA treated samples, the average values (with standard deviation, SD) for short-circuit current density (J_{SC}), open-circuit voltage (V_{OC}), fill factor (FF), and PCE are 22.38 ± 0.34 mA cm^{-2}, 1.079 ± 0.014 V, 0.795 ± 0.006%, and 19.20 ± 0.16%, respectively (SI Table S1). In a comparison to the values for the solar cells with PbI_2–HMPA treatment, a smaller PCE of 17.79 ± 0.25% is obtained from the nontreated devices, as well as a J_{SC} of 22.32 ± 0.47 mA cm^{-2}, a V_{OC} of 1.052 ± 0.009 V, and a FF of 0.758 ± 0.011. As observed in Figure 3c, all the photovoltaic parameters of the PbI_2–HMPA treated solar cells show higher average values and a smaller standard deviation (except the V_{OC}) over those of nontreated devices. These data clearly support again that the PbI_2 left at the interface due to PbI_2–HMPA treatment before the perovskite deposition is beneficial for improving the performance of a solar cell.

A direct comparison of the J–V curves from the best devices of each group is shown in Figure 3d. A significantly improved V_{OC} and an exceptionally high FF of 0.801 are measured with the PbI_2–HMPA treated device. As a result, a remarkable PCE of 19.02% is obtained from averaging the reverse scanned data of J_{SC} = 22.53 mA cm^{-2}, V_{OC} = 1.08 V, FF = 0.801, and PCE = 19.50% and the forward scanned data (J_{SC} = 22.38 mA cm^{-2}, V_{OC} = 1.08 V, FF = 0.767, and PCE of 18.54% see Figure 3f, SI Table S2). Compared with the counterpart from the nontreated group, this represents an almost 10% improvement in PCE and decreased hysteresis index[46] (1.07 > 1.05). This result represents the highest solar performance based on $CH_3NH_3PbI_3$ and a polymer HTM. The incident photon-to-current efficiency (IPCE) (Figure 3f) of the champion devices as a function of wavelength shows a very broad plateau of over 80% between 400 and 740 nm, yielding an integrated J_{SC} value of 22 mA cm^{-2} that is in a good agreement with that measured by J–V curves (Figure 3f). We believe that this first demonstration of PbI_2–HMPA treatment can be considered as a promising approach to improve the overall performance of the PSCs.

Ion conduction[47] or ion migration[48−50] is well-known for lead halide perovskite materials and is believed to be one intrinsic reason for photocurrent hysteresis and the instability of perovskite solar cells. Due to the extremely low iodine migration activation energies (0.1 eV), this phenomenon can happen spontaneously[51] or be induced by an electric field[48,52,53] or light.[50] Depending on the fabrication conditions, it has been reported that the iodine can diffuse into the above HTM layer to different extents.[51] To shed light on the distribution of iodine and lead elements, EDX-STEM is performed on a sample with the PbI_2–HMPA treatment and a reference sample without the treatment (Figure 4). Lead is observed only in the perovskite phase (Figure 4b,f), while iodine is observed to have diffused in the HTM layer in both samples (Figure 4c,g). In both cells, the iodine almost diffused close to the gold electrode. This result emphasizes the importance of using a stable and inert electrode material like gold or carbon to avoid any reaction with iodine.

EDX line scans of lead and iodine of the selected regions of each sample are shown in Figure 4d,h. For the reference cell shown in Figure 4e–h, the average I over Pb atomic ratio is calculated to be 2.21 in the infiltrated mesoporous TiO_2 layer (at a depth from 260 to 460 nm). On the other hand, the I/Pb ratio is about 2.06 in the capping perovskite layer. This observation is in agreement with a previous XPS depth profile analysis even though values differ.[51] In the case of the PbI_2–HMPA treated solar cell, the decrease in the I/Pb ratio from the interpenetrating meso-TiO_2 layer to the capping perovskite is marginal, and the I/Pb ratio remains at a value close to 2. In combination with the GI-XRD study, the PbI_2–HMPA treatment underneath the perovskite layer leads to this constant I/Pb ratio, possibility due to reduced iodine migration from the perovskite capping layer into the mesoporous TiO_2 layer. It should be noted that the I/Pb ratio is lower than the theoretical value of 3 in the capping and infilitrated TiO_2 layers, presumably due to the migration of I into the HTM and also

DOI: 10.1021/jacs.6b08347
J. Am. Chem. Soc. 2016, 138, 14380−14387

FIB-induced damage.[54] The homogeneous I/Pb ratio may be responsible for the decrease in hysteresis, and also an increased cell stability as revealed by preliminary in situ measurements of the evolution of the PCE with time for unsealed devices kept under argon. As is shown in Figure S4, the PbI_2−HMPA treated perovskite solar cells exhibited much slower efficiency deterioration over 150 h when compared to the reference devices.

CONCLUSION

In summary, by using a modified sequential deposition procedure involving a novel PbI_2−HMPA complex pretreatment, we have developed a reproducible and robust method for preparing $MAPbI_3$ based perovskite solar cells with the highest efficiencies yet reported with a polymer HTM layer. This method yields a standard deviation (SD) of less than 0.2 and an average PCE as high as 19.20% with an exceptionally high FF of 0.801. A comprehensive study by GI-XRD and TCSPC confirmed the formation of a perovskite film with a PbI_2-rich region close to the electron transport layer. This observation was ascribed to the strong interaction of HMPA with PbI_2, which successfully retarded its dissolution when depositing the perovskite layer. EDX-STEM analyses revealed more uniform I/Pb ratio in the mesoporous electron transport layer when compared to the untreated samples.

ASSOCIATED CONTENT

Supporting Information

The Supporting Information is available free of charge on the ACS Publications website at DOI: 10.1021/jacs.6b08347.

Experimental details and characterization data (PDF)

AUTHOR INFORMATION

Corresponding Authors

*peng.gao@epfl.ch
*yqfeng@tju.edu.cn
*mdkhaja.nazeeruddin@epfl.ch

Notes

The authors declare no competing financial interest.

ACKNOWLEDGMENTS

The authors acknowledge SNSF NRP 70 project, 407040_154056, and the European Union Seventh Framework Programme [FP7/2007-2013] under grant agreement 604032 of the MESO project. G.G. is supported by the cofunded Marie Skłodowska Curie fellowship, H2020 grant agreement 665667, and fund 588072. Dr. Marco Cantoni of CIME-EPFL is acknowledged for fruitful discussions about the EDX data. Mr. Manuel Tschumi is acknowledged for assistance with stability tests.

REFERENCES

(1) Gao, P.; Grätzel, M.; Nazeeruddin, M. K. *Energy Environ. Sci.* **2014**, *7*, 2448.
(2) Gao, P.; Konrad, D.; Aghazada, S.; Nazeeruddin, M. K. *Chimia* **2015**, *69*, 253.
(3) Burschka, J.; Pellet, N.; Moon, S.-J.; Humphry-Baker, R.; Gao, P.; Nazeeruddin, M. K.; Grätzel, M. *Nature* **2013**, *499*, 316.
(4) http://www.nrel.gov/ncpv/images/efficiency_chart.jpg. National Renewable Energy Laboratory Best Research-Cell Efficiencies.
(5) Lee, M. M.; Teuscher, J.; Miyasaka, T.; Murakami, T. N.; Snaith, H. J. *Science* **2012**, *338*, 643.
(6) Stranks, S. D.; Eperon, G. E.; Grancini, G.; Menelaou, C.; Alcocer, M. J. P.; Leijtens, T.; Herz, L. M.; Petrozza, A.; Snaith, H. J. *Science* **2013**, *342*, 341.
(7) Xing, G.; Mathews, N.; Sun, S.; Lim, S. S.; Lam, Y. M.; Gratzel, M.; Mhaisalkar, S.; Sum, T. C.; Grätzel, M.; Mhaisalkar, S.; Sum, T. C. *Science* **2013**, *342*, 344.
(8) Wehrenfennig, C.; Eperon, G. E.; Johnston, M. B.; Snaith, H. J.; Herz, L. M. *Adv. Mater.* **2014**, *26*, 1584.
(9) Dong, Q.; Fang, Y.; Shao, Y.; Mulligan, P.; Qiu, J.; Cao, L.; Huang, J. *Science* **2015**, *347*, 967.
(10) Sun, S.; Fang, Y.; Kieslich, G.; White, T. J.; Cheetham, A. K. *J. Mater. Chem. A* **2015**, *3*, 18450.
(11) Song, T.; Chen, Q.; Zhou, H.-P.; Jiang, C.; Wang, H.-H.; Yang, Y.; Liu, Y.; You, J.; Yang, Y. *J. Mater. Chem. A* **2015**, *3*, 9032.
(12) Nie, W.; Tsai, H.; Asadpour, R.; Blancon, J.; Neukirch, A. J.; Gupta, G.; Crochet, J. J.; Chhowalla, M.; Tretiak, S.; Alam, M. a.; Wang, H.; Mohite, A. D. *Science* **2015**, *347*, 522.
(13) Zhao, L.; Luo, D.; Wu, J.; Hu, Q.; Zhang, W.; Chen, K.; Liu, T.; Liu, Y.; Zhang, Y.; Liu, F.; Russell, T. P.; Snaith, H. J.; Zhu, R.; Gong, Q. *Adv. Funct. Mater.* **2016**, *26*, 3508.
(14) Zheng, L.; Zhang, D.; Ma, Y.; Lu, Z.; Chen, Z.; Wang, S.; Xiao, L.; Gong, Q. *Dalt. Trans.* **2015**, *44*, 10582.
(15) Yu, Z.; Sun, L. *Adv. Energy Mater.* **2015**, *5*, 1500213.
(16) Qin, P.; Paulose, M.; Dar, M. I.; Moehl, T.; Arora, N.; Gao, P.; Varghese, O. K.; Grätzel, M.; Nazeeruddin, M. K. *Small* **2015**, *11*, 5533.
(17) Oku, T.; Zushi, M.; Imanishi, Y.; Suzuki, A.; Suzuki, K. *Appl. Phys. Express* **2014**, *7*, 121601.
(18) Lee, Y. H.; Luo, J.; Humphry-Baker, R.; Gao, P.; Grätzel, M.; Nazeeruddin, M. K. *Adv. Funct. Mater.* **2015**, *25*, 3925.
(19) Leblebici, S. Y.; Leppert, L.; Li, Y.; Reyes-Lillo, S. E.; Wickenburg, S.; Wong, E.; Lee, J.; Melli, M.; Ziegler, D.; Angell, D. K.; Ogletree, D. F.; Ashby, P. D.; Toma, F. M.; Neaton, J. B.; Sharp, I. D.; Weber-Bargioni, A. *Nat. Energy* **2016**, *1*, 16093.
(20) Bi, D.; Tress, W.; Dar, M. I.; Gao, P.; Luo, J.; Renevier, C.; Schenk, K.; Abate, A.; Giordano, F.; Correa Baena, J.-P.; Decoppet, J.-D.; Zakeeruddin, S. M.; Nazeeruddin, M. K.; Gra tzel, M.; Hagfeldt, A. *Sci. Adv.* **2016**, *2*, e1501170.
(21) Kim, Y. C.; Jeon, N. J.; Noh, J. H.; Yang, W. S.; Seo, J.; Yun, J. S.; Ho-Baillie, A.; Huang, S.; Green, M. A.; Seidel, J.; Ahn, T. K.; Seok, S. Il. *Adv. Energy Mater.* **2016**, *6*, 1502104.
(22) Roldán-Carmona, C.; Gratia, P.; Zimmermann, I.; Grancini, G.; Gao, P.; Graetzel, M.; Nazeeruddin, M. K. *Energy Environ. Sci.* **2015**, *8*, 3550.
(23) Liu, F.; Dong, Q.; Wong, M. K.; Djurišić, A. B.; Ng, A.; Ren, Z.; Shen, Q.; Surya, C.; Chan, W. K.; Wang, J.; Ng, A. M. C.; Liao, C.; Li, H.; Shih, K.; Wei, C.; Su, H.; Dai, J. *Adv. Energy Mater.* **2016**, *6*, 1502206.
(24) Chen, Q.; Zhou, H.; Song, T.-B.; Luo, S.; Hong, Z.; Duan, H.-S.; Dou, L.; Liu, Y.; Yang, Y. *Nano Lett.* **2014**, *14*, 4158.
(25) Supasai, T.; Rujisamphan, N.; Ullrich, K.; Chemseddine, A.; Dittrich, T. *Appl. Phys. Lett.* **2013**, *103*, 183906.
(26) Song, T.-B.; Chen, Q.; Zhou, H.; Luo, S.; Yang, Y.; You, J.; Yang, Y. *Nano Energy* **2015**, *12*, 494.
(27) Somsongkul, V.; Lang, F.; Jeong, A. R.; Rusu, M.; Arunchaiya, M.; Dittrich, T. *Phys. Status Solidi RRL* **2014**, *8*, 763.
(28) Wang, L.; McCleese, C.; Kovalsky, A.; Zhao, Y.; Burda, C. *J. Am. Chem. Soc.* **2014**, *136*, 12205.
(29) Cao, D. H.; Stoumpos, C. C.; Malliakas, C. D.; Katz, M. J.; Farha, O. K.; Hupp, J. T.; Kanatzidis, M. G. *APL Mater.* **2014**, *2*, 091101.
(30) Liu, T.; Hu, Q.; Wu, J.; Chen, K.; Zhao, L.; Liu, F.; Wang, C.; Lu, H.; Jia, S.; Russell, T.; Zhu, R.; Gong, Q. *Adv. Energy Mater.* **2016**, *6*, 1501890.
(31) Mosconi, E.; Grancini, G.; Roldán-Carmona, C.; Gratia, P.; Zimmermann, I.; Nazeeruddin, M. K.; De Angelis, F. *Chem. Mater.* **2016**, *28*, 3612.
(32) Wharf, I.; Gramstad, T.; Makhija, R.; Onyszchuk, M. *Can. J. Chem.* **1976**, *54*, 3430.

DOI: 10.1021/jacs.6b08347
J. Am. Chem. Soc. 2016, 138, 14380−14387

(33) Wakamiya, A.; Endo, M.; Sasamori, T.; Tokitoh, N.; Ogomi, Y.; Hayase, S.; Murata, Y. *Chem. Lett.* **2014**, *43*, 711.
(34) Wu, Y.; Islam, A.; Yang, X.; Qin, C.; Liu, J.; Zhang, K.; Peng, W.; Han, L. *Energy Environ. Sci.* **2014**, *7*, 2934.
(35) Yang, W. S.; Noh, J. H.; Jeon, N. J.; Kim, Y. C.; Ryu, S.; Seo, J.; Seok, S. Il. *Science* **2015**, *348*, 1234.
(36) Jeon, N. J.; Noh, J. H.; Kim, Y. C.; Yang, W. S.; Ryu, S.; Seok, S. Il. *Nat. Mater.* **2014**, *13*, 897.
(37) Ahn, N.; Son, D. Y.; Jang, I. H.; Kang, S. M.; Choi, M.; Park, N. G. *J. Am. Chem. Soc.* **2015**, *137*, 8696.
(38) Jo, Y.; Oh, K. S.; Kim, M.; Kim, K.-H.; Lee, H.; Lee, C.-W.; Kim, D. S. *Adv. Mater. Interfaces* **2016**, *3*, 1500768.
(39) Ooyama, Y.; Inoue, S.; Nagano, T.; Kushimoto, K.; Ohshita, J.; Imae, I.; Komaguchi, K.; Harima, Y. *Angew. Chem., Int. Ed.* **2011**, *50*, 7429.
(40) Gutmann, V. *The Donor-Acceptor Approach to Molecular Interactions*; Springer: Boston, MA, 1978.
(41) Day, M. C.; Medley, J. H.; Ahmad, N. *Can. J. Chem.* **1983**, *61*, 1719.
(42) Abe, Y.; Ozutsumi, K.; Ishiguro, S.-I. *J. Chem. Soc., Faraday Trans. 1* **1989**, *85*, 3747.
(43) Normant, H. *Angew. Chem., Int. Ed. Engl.* **1967**, *6*, 1046.
(44) Kim, H.-S.; Lee, C.-R.; Im, J.-H.; Lee, K.-B.; Moehl, T.; Marchioro, A.; Moon, S.-J.; Humphry-Baker, R.; Yum, J.-H.; Moser, J. E.; Grätzel, M.; Park, N.-G. *Sci. Rep.* **2012**, *2*, 591.
(45) Zhou, Y.; Vasiliev, A. L.; Wu, W.; Yang, M.; Pang, S.; Zhu, K.; Padture, N. P. *J. Phys. Chem. Lett.* **2015**, *6*, 2292.
(46) Zhang, F.; Ma, W.; Guo, H.; Zhao, Y.; Shan, X.; Jin, K.; Tian, H.; Zhao, Q.; Yu, D.; Lu, X.; Lu, G.; Meng, S. *Chem. Mater.* **2016**, *28*, 802.
(47) Yang, T.-Y.; Gregori, G.; Pellet, N.; Grätzel, M.; Maier, J. *Angew. Chem.* **2015**, *127*, 8016.
(48) Yuan, Y.; Wang, Q.; Shao, Y.; Lu, H.; Li, T.; Gruverman, A.; Huang, J. *Adv. Energy Mater.* **2016**, *6*, 1501803.
(49) Yuan, Y.; Huang, J. *Acc. Chem. Res.* **2016**, *49*, 286.
(50) deQuilettes, D. W.; Zhang, W.; Burlakov, V. M.; Graham, D. J.; Leijtens, T.; Osherov, A.; Bulović, V.; Snaith, H. J.; Ginger, D. S.; Stranks, S. D. *Nat. Commun.* **2016**, *7*, 11683.
(51) Matteocci, F.; Busby, Y.; Pireaux, J.-J.; Divitini, G.; Cacovich, S.; Ducati, C.; Di Carlo, A. *ACS Appl. Mater. Interfaces* **2015**, *7*, 26176.
(52) Meloni, S.; Moehl, T.; Tress, W.; Franckevičius, M.; Saliba, M.; Lee, Y. H.; Gao, P.; Nazeeruddin, M. K.; Zakeeruddin, S. M.; Rothlisberger, U.; Graetzel, M. *Nat. Commun.* **2016**, *7*, 10334.
(53) Azpiroz, J. M.; Mosconi, E.; Bisquert, J.; De Angelis, F. *Energy Environ. Sci.* **2015**, *8*, 2118.
(54) Xiao, C.; Li, Z.; Guthrey, H.; Moseley, J.; Yang, Y.; Wozny, S.; Moutinho, H.; To, B.; Berry, J. J.; Gorman, B.; Yan, Y.; Zhu, K.; Al-Jassim, M. *J. Phys. Chem. C* **2015**, *119*, 26904.

DOI: 10.1021/jacs.6b08347
J. Am. Chem. Soc. 2016, 138, 14380−14387